Chapter 18

Standardization and Normalization of Data from Laser Ablation Inductively Coupled Plasma Mass Spectrometry

Ricarda Uerlings, Andreas Matusch and Ralf Weiskirchen

Additional information is available at the end of the chapter

http://dx.doi.org/10.5772/64769

Abstract

Laser ablation inductively coupled plasma mass spectrometry is a useful technique for the precise determination of major, minor and trace element distributions or isotope ratios in solid samples and biological tissue sections. However, measured ion intensities of selected mass-to-charge ratios, may vary considerably from run to run and might also underlie non-linear drift within a run. Therefore, beside the calibration of the measurement, normalization of ion intensities to a reference such as an internal standard is necessary. Other strategies use an endogenous reference element of which a homogenous distribution in the sample is assumed, or derive a more complex reference parameter from a given dataset. Generally, normalization methods depend on the experimental setup and sample material and are usually based on one or few isotopes or the total ion current. This chapter reports different normalization methods that either used a separate reference value for each data point – constituting a pixel in the isotope image – or used a constant normalization factor per measurement run. In conclusion, normalization is essential to minimize deviations of element concentrations due to measurement-related fluctuations. Normalization and definition of an area of interest are powerful tools to obtain high-contrast isotope images with absolute element concentrations.

Keywords: standardization, normalization, spiking, visualization, quantification, ELAI

1. Introduction

Laser ablation inductively coupled plasma mass spectrometry (LA-ICP-MS) is today a well-established technique for direct analysis of solid samples [1, 2]. It allows the uncomplicated elemental analysis of many different kinds of sample materials with inexpensive preparation methods. It can be used for the precise determination of major, minor, and trace element distributions or isotope ratios and is therefore already applied in many research fields [3, 4]. The basic principle of LA-ICP-MS is the multielement analysis of a mostly solid sample. The sample is placed in an ablation chamber purged with a constant argon gas flow and ablated line-by-line with a laser beam focused on the sample surface. The amount of ablated material and thus the composition of the gas phase are highly depending on the sample and laser properties [5, 6]. The aerosol consisting of the ablated material and argon is transported to the plasma torch for evaporation, atomization, and ionization [7]. After refocusing the gas stream in the sampler/skimmer interface, the generated ions are separated in the quadrupole mass spectrometer according to their mass-to-charge (m/z) ratio. The acquired signal-ion intensities are then measured and recorded as a continuous list of data points without any trigger signal indicating the line shift. This is necessary because the laser ablation unit and the mass spectrometer work independently from each other [8].

In LA-ICP-MS measurements, the ion intensities depend on many parameters. Since it is not possible to maintain perfectly constant conditions per sample and throughout a measurement run, the obtained data have to be normalized allowing the comparison of absolute element concentrations [9, 10]. There are several ways for normalization that depend on the sample material and the experimental setup. Common normalization methods [10] are either based on one isotope, the total ion current (TIC), or on selected isotopes that should represent the ion current attributable to the sample matrix termed extracted ion current (EIC). The use of internal standards as reference is desirable, but challenging with respect to the choice of a matching material and to its application or introduction [10]. Normalization can either be performed using a separate reference for each data point or a normalization factor constant throughout a measurement run or sample. In addition, for the calibration of the laser ablation process, matrix-matched standards are essential to compensate changes in the amount of ablated material even if the concentration remains constant [5].

In this chapter, different normalization methods were tested and compared:

- sum of all measured isotopes (more or less reflecting "total ion current“, TIC),
- sum of different selected isotopes ("extracted ion current“, EIC),
- different homogeneously distributed isotopes as reference,
- pixel per pixel normalization versus overall factor normalization,
- masking of background data.

The final generation of element distribution maps from the different normalization methods was done with the aid of Excel Laser Ablation Imaging (ELAI) representing a software tool that is based on Microsoft Excel 2007 Visual Basic for Applications. This software is freely

http://dx.doi.org/10.5772/64769

customizable and allows fast and easy semi-manual image generation and normalization without any further additional commercial software [8].

2. Material and methods

2.1. Sample preparation

Mice organs (brain and liver) were cryo-cut into 30 μm slices with a standard research cryostat (CM3050 S, Leica Biosystems, Wetzlar, Germany) at −18°C box temperature and −16°C object temperature. In brief, the frozen organ was fixed on a sample holder with Tissue-Tek® O.C.T. compound (Sakura Finetek Europe B.V., The Netherlands). Slices were thaw-mounted onto StarFrost® adhesive microscope slides (Waldemar Knittel Glasbearbeitungs GmbH, Braunschweig, Germany), dried, and stored at room temperature until used for LA-ICP-MS measurement.

2.2. Measurement setup

The LA-ICP-MS measurements were performed using a quadrupole-based ICP-MS (XSeries 2, Thermo Fisher Scientific, Bremen, Germany) without operating the collision cell. The Nd:YAG laser ablation unit (New Wave UP 213, New Wave, Fremont, CA, USA) was coupled directly to the ICP-MS. Measurement parameters such as RF power and gas flow were optimized for each sample with a daily performance test. Typical LA-ICP-MS measurement parameters that we used in our experiments for simultaneous detection of 21–29 different isotopes were: RF power, 1400–1600 W; carrier gas flow, 0.85–1.05 l/min; dwell time per isotope, 0.02–0.3 s; maximal energy at sample surface, > 3 mJ; fluence at sample surface, >30 J/cm^2; scan speed, 60–90 μm/s; spot size, 30 μm; and *y*-distance between the center of the lines, 60 μm, respectively. To keep the integration time of the mass spectrometer as low as possible and for receiving a high spatial resolution in the future image, only isotopes of interest were selected. The dwell time was adjusted to the sensitivity of the detector for each selected isotope.

For the measurement, the glass slide bearing the sample tissue section was positioned on the *xyz*-stage in the laser ablation chamber and moved into the focus plain (*z*-direction) of the laser beam. Within the focus correction option, the *z*-position was adjusted to the starting and ending point of every line to compensate minor variations in inclination and tilt of the sample. The ablation was performed line by line with a continuous motion in the *x*-direction and a discontinuous motion in the *y*-direction. At the end of each line, the laser was interrupted and moved back to the zero *x*-position with *y*-offset of 30 μm to the next line, while sample material was continuously transported to the mass spectrometer. The primary output data were a continuous list of ion intensities with no trigger signal indicating line shifts, because the mass spectrometer operated independently from the laser unit.

Before each measurement, the LA-ICP-MS was equilibrated to obtain constant conditions. Therefore, the ablation chamber was washed by constant carrier gas flow for about one hour to remove air entered during loading. As a function of equilibration and washing, *y*-drifts

occurred in some data sets, but also during prolonged measurement runs, i.e., over 12 h. For calibration, matrix-matched standards were measured at the end of the same run. These were produced from homogenized tissue of a homologous organ spiked with different concentrations of a standard solution [11]. Sample and standard were present at separate slides positioned side by side into the chamber.

For image generation, the LA-ICP-MS raw data of individual measurements were copied into a standardized Excel summary file, whereupon the user-defined functions (UDF) of ELAI could be accessed. Once the image dimensions (line length) have been found, the absolute element concentrations of each data point were determined from its ion intensity and the slope of a six-point calibration curve. The software tool "ELAI" [8] that we have recently developed is open software offering free customizable semimanual image generation. The complete program, including detailed documentation for installation and disclosure of all program codes is freely available and can be downloaded from the supplementary material of [8].

3. Results

Normalization requires a reference element or another parameter which is relatively homogeneous distributed throughout the sample and standard tissue sections. The concentration of a given pixel (C_{px}) is then calculated according to Eq. (1), whereby $\bar{r}_{Std}$ is the reference parameter averaged across the calibration standard measurement and r_{px} the reference parameter of the respective pixel, I_{px} the ion intensity of the isotope (m/z) of interest of the respective pixel, and m the slope of the calibration line. All these parameters are given as net values after subtraction of the respective glass background.

In the ideal case, when equal conditions apply for the considered pixel and the standard, the normalization factor $\bar{r}_{Std}/r_{px}$ becomes one when the normalization reference is one single isotope $\bar{r}_{Std}$ and r_{px} correspond to the net ion intensity thereof. In case of TIC as normalization reference, r is the sum of all ion intensities, in case of EIC the sum of the selected isotopes. When the reference parameter does not enter per pixel, but is averaged throughout the sample, r_{px} becomes constant ($\bar{r}_{px}$).

$$C_{px} = \frac{\bar{r}_{Std}}{r_{px}} \frac{I_{px}}{m} \tag{1}$$

TIC as a reference should also comply with the requirements to homogeneity and constancy in concentration throughout samples of the same type. **Figure 1** shows that after applying a TIC-based normalization strategy, the absolute element concentrations and the background noise are reinforced inversely proportional to the TIC and thus become distorted. The TIC shows a high dependence to the structure of the sample tissue because it is dominated by the

http://dx.doi.org/10.5772/64769

intensities of potassium (^{39}K, **Figure 2**) in measurements of liver and brain tissue. Additionally, for potassium despite low dwell times selected, saturation effects of the detector may occur in the ICP-MS. For these reasons, TIC-based normalization does not confer a significant gain of biological information.

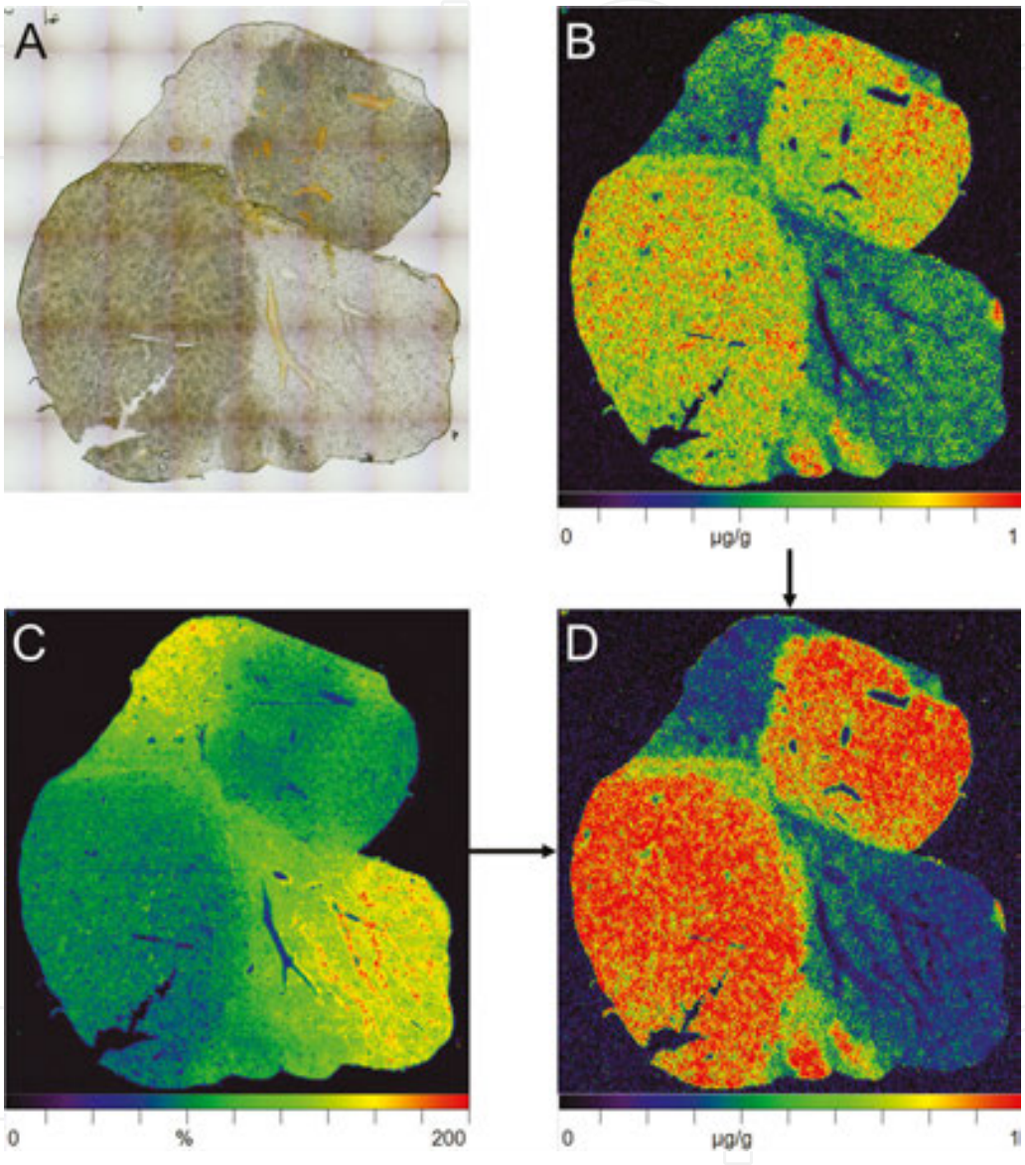

Figure 1. Normalization of ^{55}Mn in tumorous mouse liver tissue. (A) Depicted is the original liver tissue with normal hepatocytes (*dark tissue*), blood vessels, and tumors (*bright tissue*). The not normalized image of ^{55}Mn (B) shows higher manganese concentrations in regions containing normal tissue architecture than in the tumors and very low manganese concentrations in the blood vessels. (C) The pixelwise TIC divided by the average TIC of the calibration standard that is given in %. The higher signal in the tumor regions is due to the lower water content and therefore a higher amount of dry material in a given area of the slide. Pixelwise division of image (B) by image (C) results in the TIC-normalized image of ^{55}Mn that is depicted in (D).

For an EIC-based normalization strategy, a set of the most homogeneously distributed isotopes was chosen. These comprised carbon, magnesium, silicon, and sulfur (**Figure 3**).

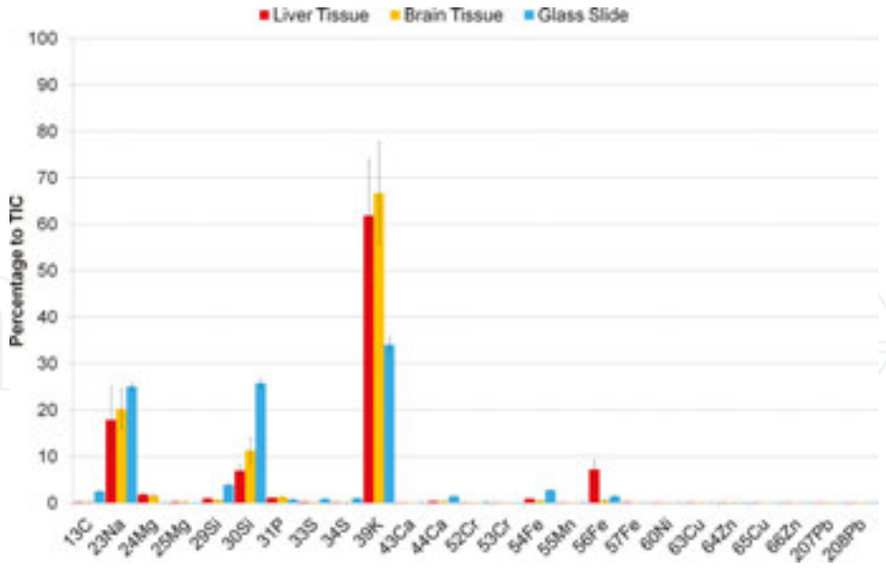

Figure 2. Percentage contribution of isotope intensities to the TIC in liver and brain tissue and to the background signal of the glass slide. The error bars indicate the standard deviation (SD) throughout all data points of the sample.

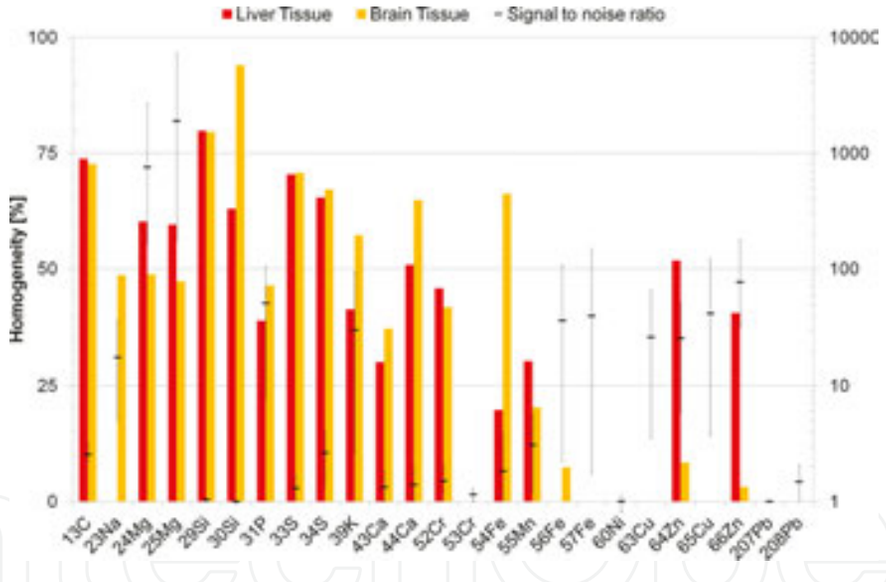

Figure 3. Homogeneity of the isotope distribution in the liver and brain tissues and the glass slide. The signal-to-noise ratio is logarithmically scaled on the secondary *y*-axis with error bars representing the range of the average signal-to-noise ratio in different measurements.

Silicon originates from the partially ablated glass slide surface subjacent to the sample. In blank background areas, the signal-to-noise ratio was about one. Silicon could therefore be a good candidate as an internal standard. However, the Si signal nonlinearly depends on the geometry of laser spot, focus, and tissue laying over the glass surface. The extreme cases are subtotal ablation of the tissue and no ablation of glass and deep ablation of glass and sparkling of tissue fragments to the side. Furthermore, the most abundant Si isotopes ^{28}Si and ^{29}Si interfere with bi-atomic $^{14}N_2$ and $^{14}N^{15}N$. In liver and brain tissue, carbon and sulfur also show a good

http://dx.doi.org/10.5772/64769

homogeneity with moderate signal-to-noise ratios for ^{13}C and ^{34}S. ^{33}S is homogeneously distributed in both sample types, but its signal-to-noise ratio is only slightly above one, making the image of ^{33}S in general very noisy. Although magnesium seems relatively homogeneously distributed in the liver and brain tissue and its signal-to-noise ratio is very high, it is not suitable for normalization because it cannot be assumed to be similar concentrated in samples of the same type. For this reason, all other metals were also omitted, independent from their homogeneities and signal-to-noise ratios. Former measurements also showed biologically and structurally meaningful and heterogeneous distributions of that magnesium, other metals and phosphorus. Therefore, these were considered unsuitable for normalization. In conclusion, taking into account homogeneity, signal-to-noise ratio and constancy of concentration, only silicon, carbon, and sulfur qualified for an extracted ion current.

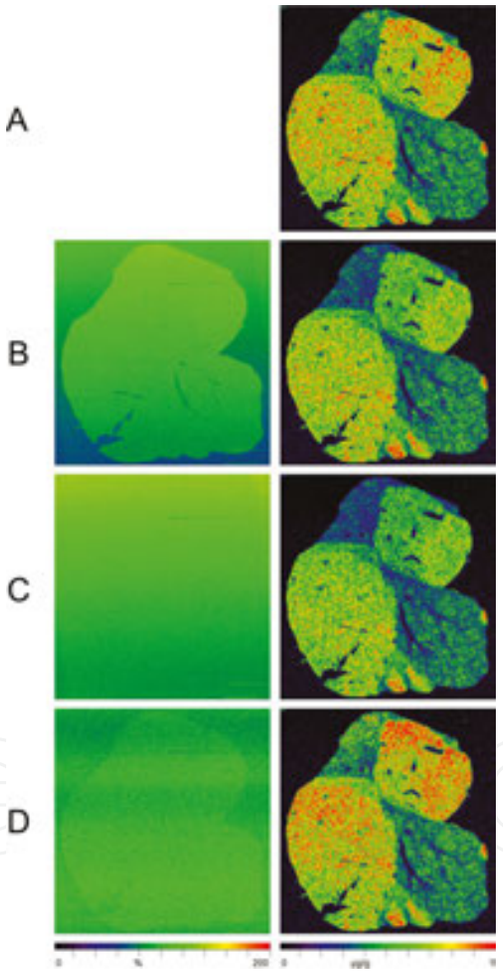

Figure 4. Normalization of ^{55}Mn in tumorous mouse liver. (A) Depicted is the non-normalized image of absolute manganese concentrations. Left images present the normalization reference images, right images the normalized manganese concentrations based on the EIC (B), ^{30}Si (C), and ^{29}Si (D).

Figure 4 shows different normalization methods for ^{55}Mn, again in comparison to the non-normalized image (**Figure 4A**) generated from absolute concentrations. The EIC image contains the summarized intensities of ^{13}C, ^{29}Si, ^{30}Si, ^{33}S, and ^{34}S relative to the respective sum

extracted from the standard measurement. Since the EIC image (**Figure 4B**) shows slightly decreasing intensities (a signal drift) from the top to the bottom, the EIC-normalized image of ^{55}Mn shows too low absolute concentrations in the upper half of the image. However, the lower half of the image looks similar to the not normalized image. The same effect is seen in the image of ^{30}Si and the corresponding normalized image of ^{55}Mn (**Figure 4C**). Since the EIC is dominated by the intensities of ^{30}Si (see below), both methods produce similar results. Additionally, since the normalization factor ($\bar{r}_{Std}/r_{px}$) for ^{30}Si was lower than for the EIC, the overall concentrations in the ^{30}Si-normalized image were lower compared to the EIC and to the non-normalized image. The opposite effect can be seen in ^{29}Si-based normalization (**Figure 4D**), where overcorrection of the vertical drift and overestimation of overall concentrations occurred. Additionally, the image of $m/z = 29$ shows slightly increased intensities over sample covered areas pointing to interferences of ^{29}Si and ^{14}N^{15}N [12].

A higher contribution of ^{13}C/^{16}O can be excluded as in this case also at $m/z = 30$, a contribution of ^{12}C/^{18}O should be observed. The contribution of five different ion intensities (^{13}C, ^{29}Si, ^{30}Si, ^{33}S, and ^{34}S) to the EIC is resumed in **Figure 5**.

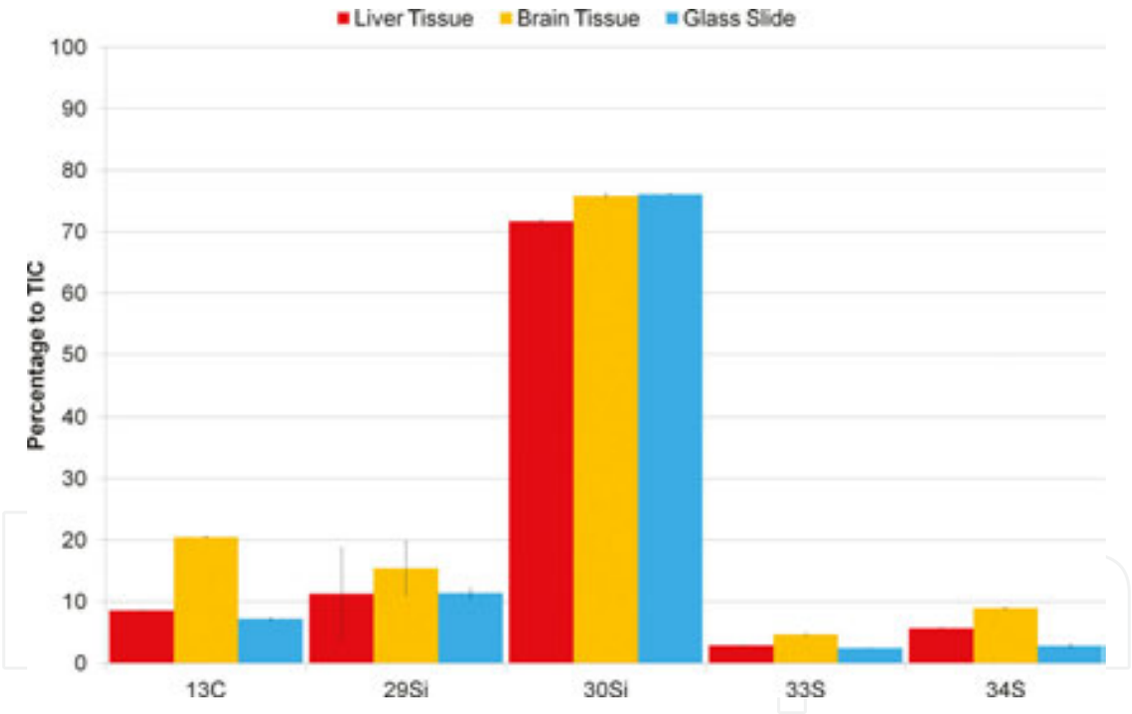

Figure 5. Contribution of isotope intensities to the EIC for liver and brain tissue and the glass background. Error bars indicate the standard deviation of all pixels across the area considered.

Figure 6 presents the results for normalization to other reference isotopes, which are also contained in the set for EIC. In comparison to the not normalized image of ^{55}Mn (**Figure 6A**), the concentrations of the normalized images that are based on ^{13}C (**Figure 6B**), ^{33}S (**Figure 6C**), and ^{34}S (**Figure 6D**) show no distortion and look much more similar than the not normalized image. This is due to the fact that the respective elements (^{13}C, ^{33}S, and ^{34}S) are more homogeneously distributed and only differ in the background height and image noise.

http://dx.doi.org/10.5772/64769

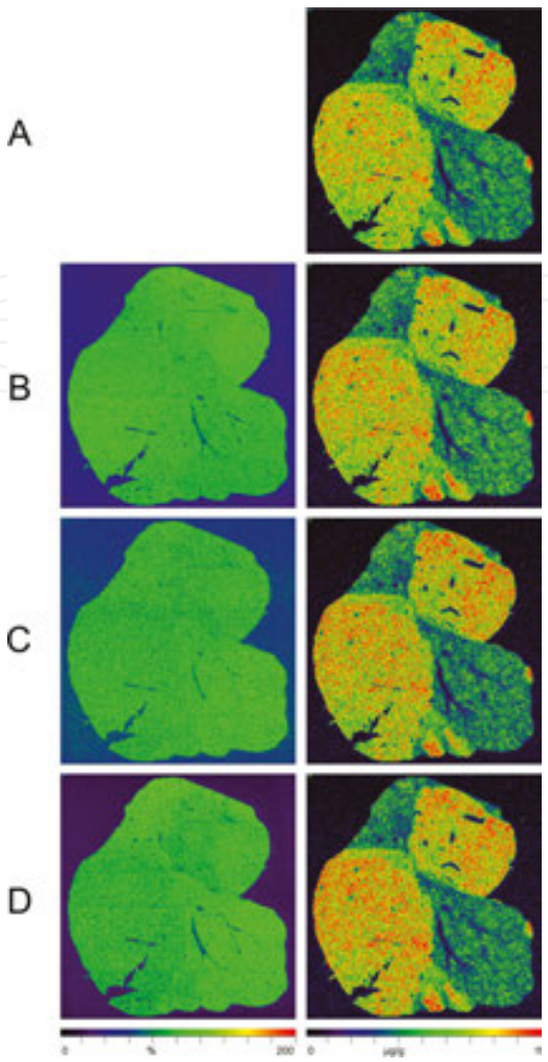

Figure 6. Normalization of ^{55}Mn in tumorous mouse liver tissue. (A) Depicted is the not normalized image of absolute manganese concentrations. Images on the left present the normalization reference images, the images on the right the normalized manganese concentrations based on ^{13}C (B), ^{33}S (C), and ^{34}S (D) resulting from pixelwise division of image (A) by the respective left hand images.

Consequently, normalization that is based EIC of carbon and sulfur can be a useful method to obtain comparable absolute concentrations for all measurements of one specific sample type. Since ^{13}C and ^{34}S normally provide higher intensities than ^{33}S, with an additionally good signal-to-noise ratio (cf. **Figure 3**), normalization with only ^{13}C or ^{34}S is a good and easy to handle option for organic tissue. The final election for ^{13}C or ^{34}S depends on which element is more homogeneous in the analyzed tissue type. However, due to the lower water and therefore higher C and S content in tumor regions, Mn concentrations were underestimated there. This effect is especially obvious in the example depicted in **Figure 6D**.

The principal advantage of pixel per pixel normalization is the attenuation of signal drift and occasionally occurring line artifacts that are caused by sparkling of insufficiently adhering material fragments (**Figure 7A–C**) and therefore appearing at all sample related *m*/*z* in parallel

or intervention by the user. Of course, drifts and artifacts cannot be overcome by a constant normalization factor (**Figure 7D**). On the other hand, pixelwise normalization introduces and multiplies noise, especially if the divisor image is not graphically smoothed (**Figure 7E**).

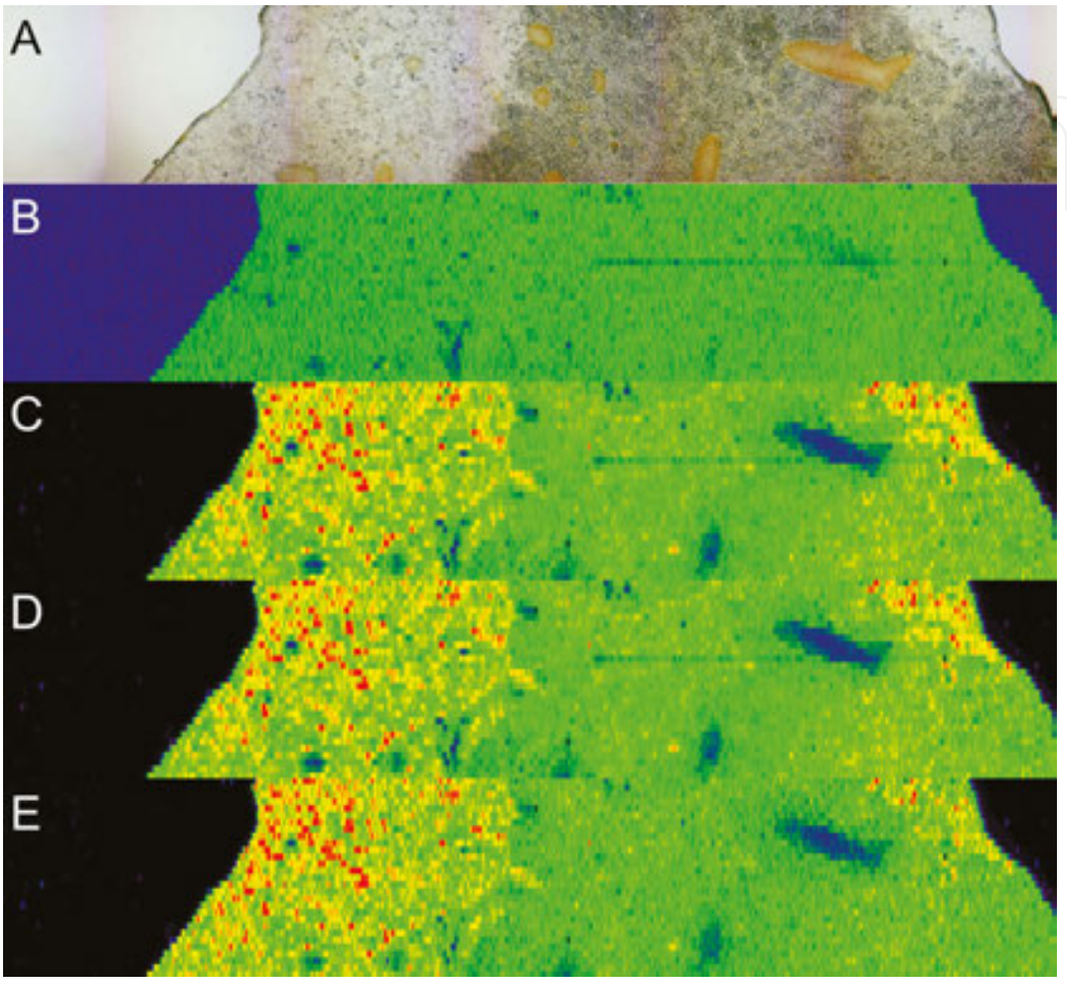

Figure 7. Image detail containing a line artifact (*dark stripe*) that occurred for all measured isotopes. (A) Depicted is the light microscopic image of the analyzed tissue sample. Exemplarily shown are the images generated for (B) ^{13}C, (C) ^{24}Mg (not normalized), (D) ^{24}Mg (normalized with a constant factor based on ^{13}C), and (E) ^{24}Mg normalized pixel per pixel based on ^{13}C.

In measurements of isotopes with low signal-to-noise ratios (i.e., the averaged ion intensity divided by the standard deviation in areas covered by sample/in glass background areas) or elements that are concentrated just above the detection limit, the normalization could increase the background and therefore make the evaluation of the isotope image more difficult. Here, a correct determination and subtraction of the glass background has special impact. A series of works used image analysis software for hand drawing regions of interest (ROIs) including glass background and read out of average values thereof [10].

In our studies, we used a histogram function within Excel Visual BASIC to identify background pixels and for segmentation of a background and a foreground mask. In typical measurements,

http://dx.doi.org/10.5772/64769

there is a discontinuous histogram showing a bimodal intensity distribution with a clear cut between the sample and background pixel populations. In the "de-spiked data," the scaling was weighted to the mid range. Most data points assigned to the sample were in the range of 50–60% of the maximum percentage ("Max%" in **Figure 8**). Background data points were in the range of 20–30% of the maximum percentage in typical images. The output of the integral of the histogram "cumulative %" allows additional control of plausibility, whether this corresponds to the visual impression of the fraction of background (**Figure 8**). In a second step, the pixels assigned to sample (foreground) by cutting the histogram are further evaluated individually. Therefore, at least one neighbored data point (i.e., left, right, above, and below) must also be greater than the threshold value, otherwise the considered data point is assigned as spike and not added to the final mask.

The mask should edge the sample tissue clearly and ideally exclude cracks and holes in the tissue. If a mask generation is performed based on an image with inhomogeneous distribution, many data points in the sample tissue could be falsely excluded (**Figure 9A**). In contrast to this, the resulting mask may contain many data points that do not belong to the sample tissue, but to the background noise, if the reference image for the mask generation has a low signal-to-noise ratio (**Figure 9B**). Thus, analog to the determination of the normalization factor, best results for the mask can be achieved with a homogeneous reference image and a good signal-to-noise ratio (**Figure 9C**). Once the optimum area of interest is found, it is converted into a binary image, in which all background data points are colored black and assigned a value of "0.01" and all sample tissue data points are colored gray and set to "1."

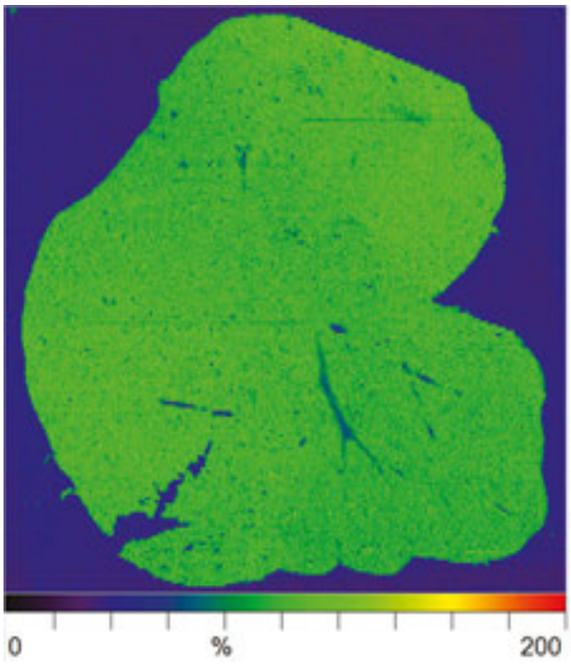

Max%	class	abundance	cumulative %
0.1	0	3	0%
1	2	0	0%
5	10	0	0%
10	20	3	0%
20	40	29858	25%
30	60	8602	32%
40	80	1618	33%
50	100	38117	65%
60	120	42027	100%
70	140	522	100%
80	160	8	100%
90	180	3	100%
95	190	0	100%
100	200	0	100%

Figure 8. Image and histogram of ^{13}C ion intensities in mouse liver weighted to the mid range. Please note the clear separation of pixel populations from background (*blue*, 30% and below) and sample (*green*, 50% and above).

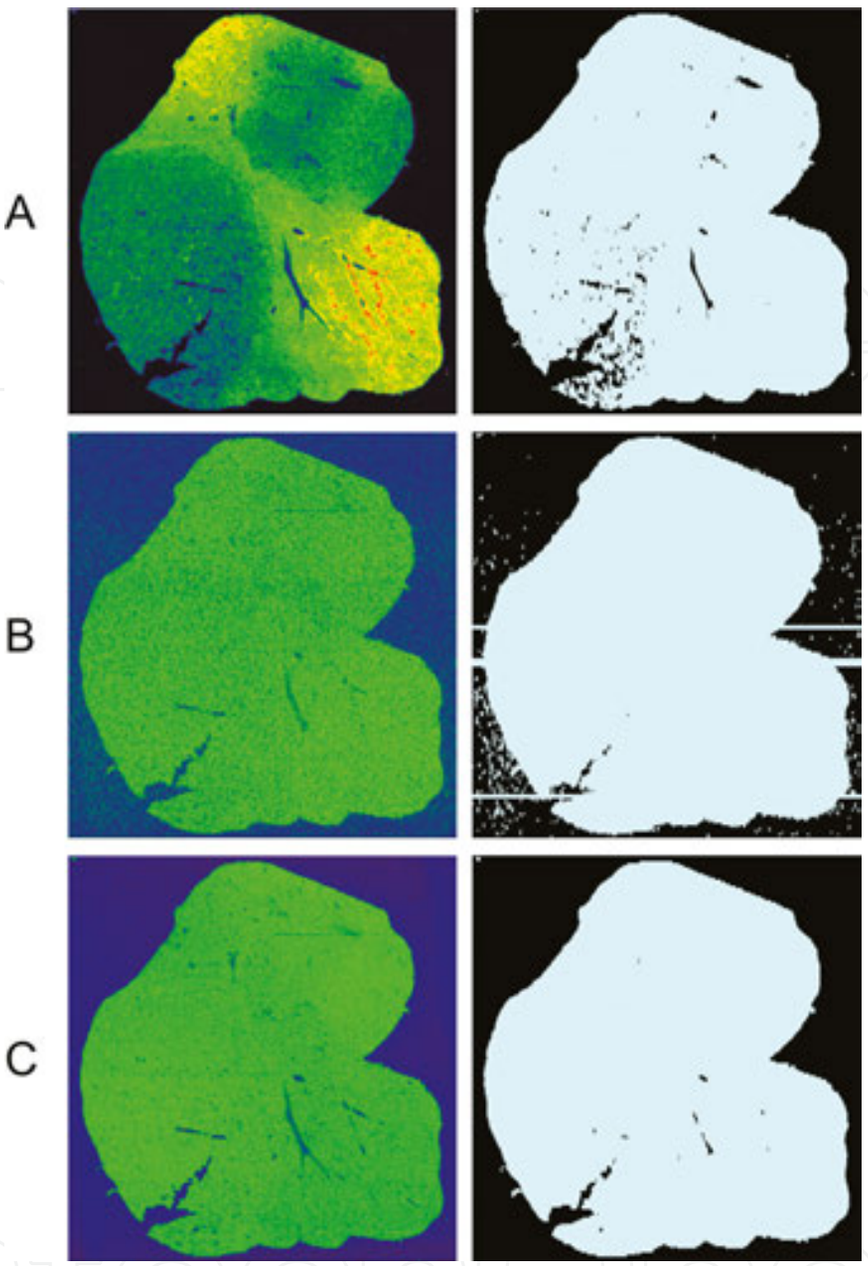

Figure 9. Mask generation based on different reference images. Please note the differences in the masks that were prepared with images that are based on (A) the total ion current (TIC), (B) ^{33}S, and (C) ^{13}C.

Thus, all background data points outside of the area of interest are divided by hundred and therefore significantly reduced. On the other hand, all sample tissue data points retain their concentration level, but the achievable contrast between sample tissue and background is much higher.

Of course, there are also some limitations in the generation of images from the measured data sets. Since the length of a formula in Excel 2007 is limited to 1000 characters [13] and a typical data set contains more than 32,000 data points, it is not useful to process every single cell position of all data points that meet the requirements. Therefore, for data compression,

http://dx.doi.org/10.5772/64769

matching data points are combined into blocks whose cell coordinates are stored in a two-dimensional matrix. For example, in the third line of an image, data points "cells(3;5)" to "cells(3;12)" fit the conditions, then the cell coordinates are saved as "E3" and "L3" and combined to "E3:L3." One line can include several blocks if the sample tissue contains any gaps. Finally, all blocks are combined in one overall area of interest and stored as cell name reference "total_mask." The mask is transferred to all previously applied images and stored for each specific image sheet. These masks can be selected in the "name bar" and used for further calculations, for example, the average element concentration in the area of interest. To visualize the mask for verification, sample data points (**Figure 10A**) are colored gray and background is colored black (**Figure 10B**). On this basis, the reference image is recalculated with reduced background (**Figure 10C**). Moreover, background masking is especially useful for reducing background noise in images of low contrast, such as of some trace elements (**Figure 10D–F**).

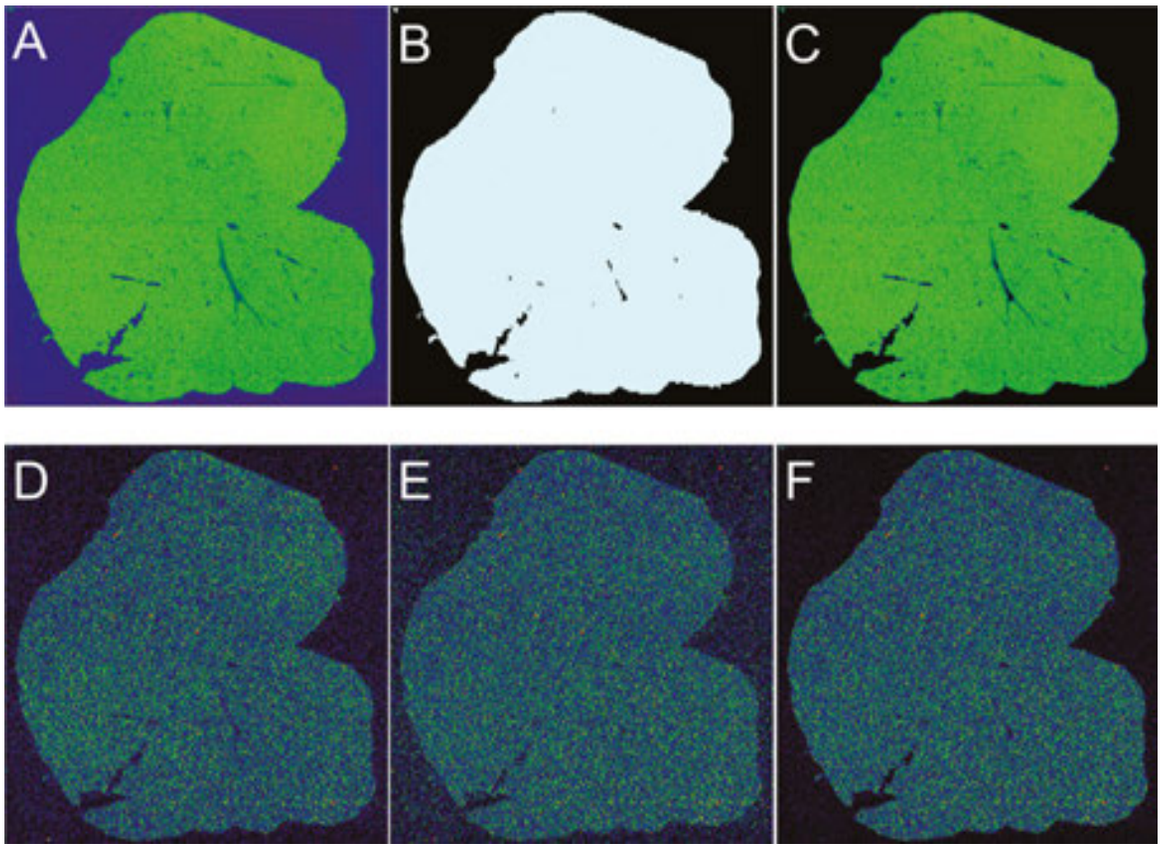

Figure 10. Creation of a foreground sample mask from the reference image. The ^{13}C measurement shown in (A) was used to prepare the mask depicted in (B). The reference image was recalculated with reduced background (C). Low concentrated ^{52}Cr (D) shows a higher background (E) after normalization based on (A), but significantly lower background (F) when normalized with (C) as normalization reference.

Pixelwise normalization can be used as a powerful tool to minimize deviations of element concentrations due to measurement-related fluctuations. Horizontal brain sections as shown

in **Figure 11** are expected to be approximately anatomically symmetrical and thus, signal drifts in the non-normalized images most likely result from insufficient washing and equilibration and also prolonged measurement times (that were here 14 h). This is of course not overcome by background subtraction and normalization with a constant factor. In contrast, pixelwise normalization reduces excessive values and increases too small intensities in relation to the reference isotope which significantly improves the image quality (**Figure 11**).

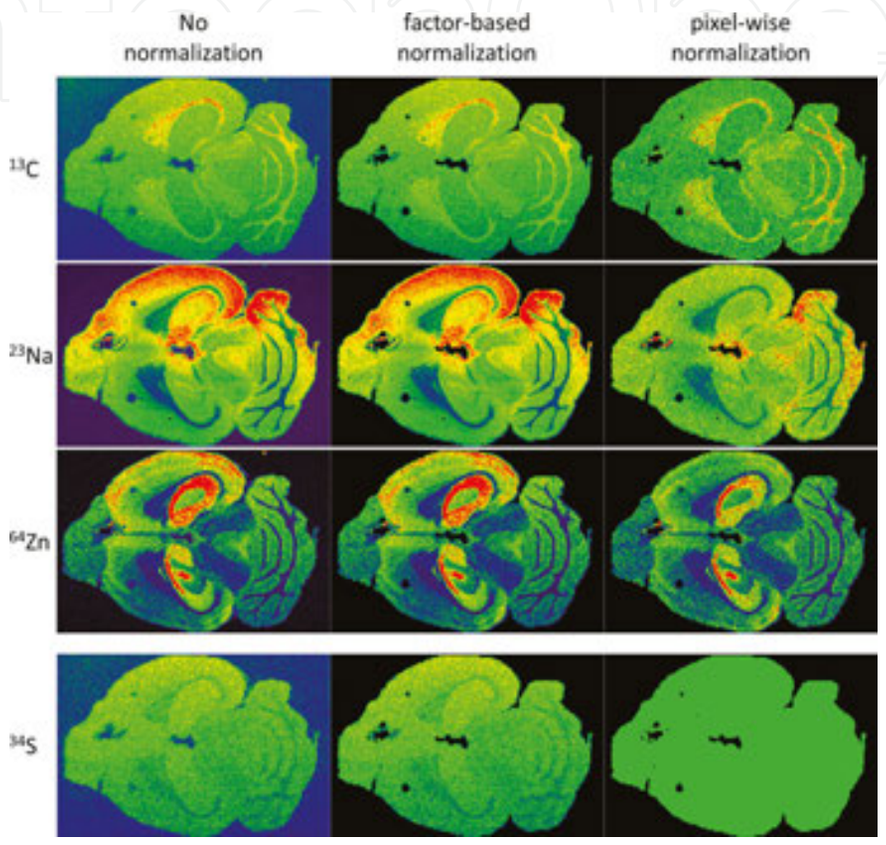

Figure 11. Comparison between images that were normalized using different strategies. Shown are non-normalized images (*left*), congruent to constant factor normalized images (*middle*), and pixelwise normalized images (*right*) of ^{13}C, ^{23}Na, and ^{64}Zn in section derived from mouse brain. The normalization was performed on the basis of the image of ^{34}S (*left*) and the corresponding area of interest (*middle*). The pixelwise normalization of ^{34}S (*right*) shows the theoretical homogeneity obtained by decreasing and increasing signal-drift distorted values.

4. Conclusion

In order to take into account that absolute element concentrations vary due to slightly different measurement conditions, normalization is essential to make data sets comparable. It is necessary to minimize deviations originated by measurement errors or measurement-related fluctuations, especially in the form of signal drifts.

Generally, normalization is highly dependent on the sample type and the selected reference, but in each case, the normalization reference should be distributed as homogeneous as

http://dx.doi.org/10.5772/64769

possible. Ideally, an internal standard is used for normalization, but this is difficult to introduce into sectioned, nonhomogenized sample material. Within narrow limits and high requirements at the constancy of ablation conditions ^{30}Si but not ^{29}Si may be used as an internal standard in the broadest sense.

TIC-based normalization proved to be not recommended for biomedical sample tissue of this study because it is dominated by inhomogeneously distributed potassium. Inhomogeneity leads to distorted absolute element concentrations due to structural and matrix effects. Mostly, one single isotope with a good homogeneity and signal-to-noise ratio is sufficient as normalization reference. EIC-based normalization underlay the same restrictions, but may be helpful if inverse variations of isotope signals such as ^{13}C, ^{33}S, and ^{34}S form a relatively homogeneous reference which cannot be achieved by one single isotope.

Moreover, factor-based normalization is completely sufficient, but device-dependent errors in the data may be attenuated with pixelwise normalization. However, pixelwise normalization may increase the image noise, especially for isotopes with low signal-to-noise ratios. In this case, the definition of an area of interest is very useful to improve the image contrast significantly.

ELAI that we use for image generation, proved as a powerful software tool, capable of quickly responding to user demands and solving variable and individual analytical questions in the area of LA-ICP-MS of tissue sections. Both, development and support of ELAI are ongoing in our laboratory.

Abbreviations

EIC	extracted ion current
ELAI	Excel Laser Ablation Imaging
LA-ICP-MS	laser ablation inductively coupled plasma mass spectrometry
m/*z*	mass-to-charge
TIC	total ion current

Acknowledgements

Ralf Weiskirchen is supported by the German Research Foundation (SFB/TRR 57, projects P13 and Q3) and the Interdisciplinary Centre for Clinical Research within the Faculty of Medicine at the RWTH Aachen University (IZKF Aachen, project E7-6). None of the funding sources were involved in the writing of the report or in the decision to submit this book chapter for publication.

Author details

Ricarda Uerlings[1], Andreas Matusch[2] and Ralf Weiskirchen[1*]

*Address all correspondence to: rweiskirchen@ukaachen.de

1 Institute of Molecular Pathobiochemistry, Experimental Gene Therapy and Clinical Chemistry, RWTH University Hospital Aachen, Aachen, Germany

2 Institute of Neurosciences and Medicine (INM-2), Forschungszentrum Jülich, Germany

References

[1] Sussulini A, Becker JS, Becker JS. Laser ablation ICP-MS: application in biomedical research. *Mass Spectrom Rev*. 2015 Sep 23. DOI: 10.1002/mas.21481.

[2] Limbeck A, Galler P, Bonta M, Bauer G, Nischkauer W, Vanhaecke F. Recent advances in quantitative LA-ICP-MS analysis: challenges and solutions in the life sciences and environmental chemistry. *Anal Bioanal Chem*. 2015;407:6593–6617. DOI: 10.1007/s00216-015-8858-0.

[3] Konz I, Fernández B, Fernández ML, Pereiro R, Sanz-Medel A. Laser ablation ICP-MS for quantitative biomedical applications. *Anal Bioanal Chem*. 2012;403:2113–2125. DOI: 10.1007/s00216-012-6023-6.

[4] Weiskirchen R, Uerlings R Laser ablation inductively coupled plasma mass spectrometry in biomedicine and clinical diagnosis. *Cell Mol Med: Open Access.* 2015;1:3.

[5] Russo RE, Mao X, Borisov OV. Laser ablation sampling. *TrAC Trends Anal Chem*. 1998;17:461–469. DOI: 0.1016/S0165-9936(98)00047-8.

[6] Limbeck A, Galler P, Bonta M, Bauer G, Nischkauer W, Vanhaecke F. Recent advances in quantitative LA-ICP-MS analysis: challenges and solutions in the life sciences and environmental chemistry. *Anal Bioanal Chem*. 2015;407:6593–6617. DOI: 10.1007/s00216-015-8858-0.

[7] Becker JS. Applications of inductively coupled plasma mass spectrometry and laser ablation inductively coupled plasma mass spectrometry in materials science. *Spectrochim Acta B.* 2002;57:1805–1820. DOI: 10.1016/S0584-8547(02)00213-6.

[8] Uerlings R, Matusch A, Weiskirchen R. Reconstruction of laser ablation inductively coupled plasma mass spectrometry (LA-ICP-MS) spatial distribution images in Microsoft Excel 2007. *Int J Mass Spectrom*. 2016;395:27–35. DOI: 10.1016/j.ijms.2015.11.010.

[9] Liu Y, Hu Z, Gao S, Günther D, Xu J, Gao C, Chen H. *In situ* analysis of major and trace elements of anhydrous minerals by LA-ICP-MS without applying an internal standard. *Chem Geol.* 2008;257:34–43. DOI: 10.1016/j.chemgeo.2008.08.004.

[10] Fonville JM, Carter C, Cloarec O, Nicholson JK, Lindon JC, Bunch J, Holmes E. Robust data processing and normalization strategy for MALDI mass spectrometric imaging. *Anal Chem*. 2012;84:1310–1319. DOI: 10.1021/ac201767g.

[11] Hare DJ, Lear J, Bishop D, Beavis A, Doble PA. Protocol for production of matrix-matched brain tissue standards for imaging by laser ablation-inductively coupled plasma-mass spectrometry. *Anal Methods*. 2013;5:1915–1921. DOI: 10.1039/c3ay26248k.

[12] May TW, Wiedmeyer RH. A table of polyatomic interferences in ICP-MS. *Atom Spectrosc*. 1998;19:150–155.

[13] Microsoft. Excel 2010 Performance: Performance and limit improvements. Available from: https://msdn.microsoft.com/en-gb/library/office/ff700514%28v=office.14%29.aspx [Accessed: 2016-06-30].

IntechOpen